CHEMISTRY OF MATERIALS

Article

pubs.acs.org/cm

Shape Evolution of “Multibranched” Mn−Zn Ferrite Nanostructures with High Performance: A Transformation of Nanocrystals into Nanoclusters

Jun Xie, Changzhi Yan, Yu Zhang,* and Ning Gu*

State Key Laboratory of Bioelectronics, Jiangsu Key Laboratory for Biomaterials and Devices, School of Biological Science and Medical Engineering, Southeast University, Nanjing 210096, P. R. China

Supporting Information

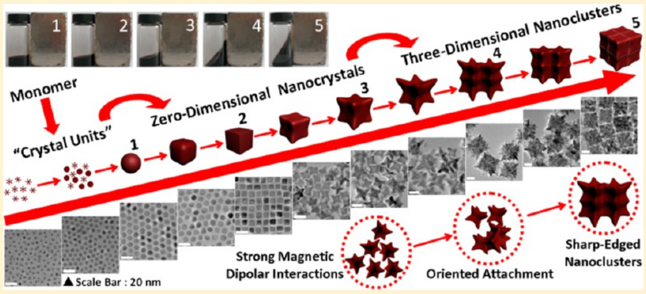

ABSTRACT: Monodisperse magnetic Mn−Zn ferrite nanostructures with various morphologies have been successfully synthesized via high-temperature decomposition of metal acetylacetonate (acac) in the presence of oleic acid (OA) and oleyamine (OAm). In a classical crystal nucleation/growth process, differential stabilization of OA on specific crystal facets may alter relative crystal growth rates, resulting in the formation of zero-dimensional (0-D) spherical, cubical, and starlike nanocrystals (ca. 9, 11, 16 nm), respectively. Furthermore, shortening nucleation duration might bring a deficient nucleation and a rapid increase in monomer concentration, which accelerates the subsequent growth process of nanocrystals, leading to the formation of the starlike nanocrystals with larger size (ca. 19−23 nm). They are further oriented to assemble reciprocally, gradually forming initial three-dimensional (3-D) “branched” nanoclusters (ca. 30−40 nm) to minimize the magnetostatic energy, owing to their size-dependent magnetic dipolar interaction. In addition, the surface-defect-induced secondary growth of the “branched” nanoclusters may considerably improve their uniformity, accompanied by the size increase in the presence of the monomers, resulting in the final “multibranched” nanoclusters with formation of sharp or obtuse edges (ca. 45−50 nm). Our study reveals the transformation of 0-D nanocrystals to 3-D nanoclusters as well as the shape evolution mechanism, which provide a versatile synthetic strategy for shape-controlled nanostructure. The multibranched nanoclusters have the higher magnetization and magnetically induced heating efficiency in an alternating current magnetic field, which can be used as promising heating agents for biomedical application.

KEYWORDS: *Mn−Zn ferrite nanostructures, shape evolution, oriented attachment, high performance*

INTRODUCTION

Magnetic nanostructure is of great scientific interest for researchers in a wide range of biomedicine applications, including magnetic resonance imaging (MRI), triggered drug release, magnetic fluid hyperthermia, and catalysis.[1] Specially, the fabrication of these nanostructures with controllable size, morphology, composition, and aggregation is even more fascinating, which may distinctly improve their surface physical/chemical properties.[2] The shape of nanostructure can be simply classified by their dimensionality. In general, zero-dimensional (0-D) magnetic nanostructures (e.g., spheres, cubes, and polyhedrons) are the most basic motifs among shaped nanocrystals.[2b,3] These individual nanocrystals (generally less than 20 nm in size) behave as a single magnetic domain and exhibit negligible remanence and coercivity in an applied magnetic field (AMF), leading to their predominant superparamagnetism, which play a critical role in mass practical applications.[1,2c,4] Unlike 0-D nanocrystals, recent successful synthetic studies of magnetic nanostructure have mostly focused on “clusters”. The peculiar structures of three-dimensional (3-D) nanoclusters based on crystal aggregation have been shown theoretically and experimentally to be able to increase their saturation magnetization,[2d,5] which are used as efficient mediators for MRI and hyperthermia in cancer treatment.[5b,c] Furthermore, the irregular nanoclusters with multiple crystal facets tend to have a larger surface area than traditional nanocrystals,[2d] which may play a dominant role in catalytic research and application.

During the past decades, some progress on the synthesis of monodisperse magnetic nanostructures with various shapes and sizes has focused on thermal decomposition of organometallic precursors,[2,3,4b] in which most of the efforts were made on tuning several critical factors, such as surfactants, metal precursors, and solvent category.[3e,6] In nanocrystals synthesis, a classical crystallization mode based on the supersaturation of solution is usually used to explain the crystal nucleation/growth

Received: June 23, 2013
Revised: August 27, 2013

dx.doi.org/10.1021/cm402036d | *Chem. Mater.* XXXX, XXX, XXX−XXX

kinetics,[7a] which plays a fundamental role in tailoring the nanocrystals with controllable sizes and shapes. In contrast, another significant mechanism named nonclassical "oriented attachment" was recently proposed.[7] The aggregation-based crystal growth theory shows its specific characteristics and roles in the formation of larger and irregular nanoclusters.

As we know, the essence of shape-controlling is tuning the growth rate in specific directions in the crystal growth process. The choice of appropriate surfactant remains an important challenge, because the surfactant can selectively bind to specific crystal facets and tunes the growing rate of crystal facets.[6a,b] For instance, oleic acid (OA) and oleyamine (OAm) as typical capping surfactants are used to stabilize the formation of magnetic nanostructures in a decomposition reaction of metal acetylacetonate (acac), which is first developed by Sun's group.[3e,6c,8] There are numerous reports on surfactant-assisted synthesis of magnetic nanostructures with varied shapes, but studies on the shape formation mechanism are in short supply. In this study, we report a shape controllable synthesis of doping Mn−Zn ferrite nanostructures (including nanocrystals and nanoclusters), one of the most intensively investigated magnetic materials with larger magnetocrystalline anisotropy and higher magnetic susceptibility, compared with Fe_3O_4, γ-Fe_2O_3, $CoFe_2O_4$, $MnFe_2O_4$, and $ZnFe_2O_4$ nanostructures,[1a,9] by modified high-temperature decomposition of iron(III) acetylacetonate [$Fe(acac)_3$], zinc(II) acetylacetonate [$Zn(acac)_2$], and manganese(II) acetylacetonate [$Mn(acac)_2$] in a high-boiling octyl ether solvent in the presence of OA and OAm. More importantly, a systematic study on the shape-controlled growth mechanism of the nanocrystals and nanoclusters based on classical crystallization and nonclassical oriented attachment theories is presented here, which may prompt a detailed understanding of the shape evolution of ferrite nanostructures with special morphologies.

■ EXPERIMENTAL SECTION

Materials. The synthesis of Mn−Zn ferrite nanostructures was carried out using standard procedures and commercially available reagents. $Fe(acac)_3$ (98%), OA ($C_{17}H_{33}COOH$, 85%), and OAm ($C_{18}H_{35}NH_2$, 90%) were purchased from Aladdin Chemical Reagent Co. Ltd. $Mn(acac)_2$ (97%) and $Zn(acac)_2$ (96%) were purchased from Alfa Aesar. Octyl ether ($C_8H_{17}OC_8H_{17}$, 95%) was purchased from J&K Chemical Reagent Co. Ltd. The commercially available reagents, including isooctane (85%), ethanol (95%), and acetone (99%), were all purchased from Sinopharm Chemical Reagent Co. Ltd. Deionized water was produced by an Aquapro water purification machine (EDI1-1001-U, Yiyang). All the chemicals were used as-received without any further purification.

Synthesis of Spherical, Cubical, and Starlike Mn−Zn Ferrite Nanocrystals. The shape-controlled nanocrystals were obtained by different molar ratios of OA to OAm without any additional reductive reagents. In representative spherical, cubical, and starlike nanocrystals synthesis, $Fe(acac)_3$ (2 mmol), $Mn(acac)_2$ (0.6 mmol), and $Zn(acac)_2$ (0.4 mmol) were placed in a 50 mL three-neck round-bottom flask in 20 mL of octyl ether, coexisting with 10 mmol of OA and 2 mmol of OAm, 7 mmol of OA and 5 mmol of OAm, or 5 mmol of OA and 7 mmol of OAm, respectively. They were mixed and stirred under a flow of N_2. The mixture was first heated to 110 °C for 30 min to remove water at a heating rate of 3 °C/min, the temperature was raised to 220 °C, and the mixture refluxed for 2 h. In succession, under N_2 flow with continuous stirring, the mixture was heated to 300 °C with a heating rate of about 3 °C/min and maintained at this temperature for up to 1 h. The black-brown mixture was precipitated, washed three times using ethanol and acetone, and was then dispersed in isooctane.

Synthesis of Self-Assemblied Mn−Zn Ferrite Nanoclusters. A similar strategy for the synthesis of Mn−Zn ferrite nanoclusters in larger sizes was proposed. A 2 mmol portion of $Fe(acac)_3$, 0.6 mmol of $Mn(acac)_2$, and 0.4 mmol of $Zn(acac)_2$ were placed in a 50 mL three-neck round-bottom flask in 20 mL of octyl ether in the presence of 5 mmol OA and 7 mmol OAm, stirred under a flow of N_2. The mixture was first heated to 110 °C at the heating rate of 3 °C/min for 30 min and then the temperature was raised to 220 °C and kept there for only 30 min. This key modification had a significant effect on the morphology of nanocrystals assemblies. Under a blanket of N_2, the mixture was further heated to reflux at 300 °C with a heating rate of about 3 °C/min for 40−60 min. After centrifugation and washing with ethanol several times, the highly purified nanoclusters dispersed in isooctane were produced.

Characterization of Mn−Zn Ferrite Nanostructures. The morphology of the nanocrystals and nanoclusters was observed using transmission electron microscopy (TEM, Tokyo JEOL) coupled with high-resolution TEM (HRTEM) and scanning electron microscope (SEM, Hitachi S-4800) with energy dispersive spectroscopy (EDS) pattern. The samples were diluted in isooctane solvent and dispersed on amorphous carbon-coated copper grids for TEM analysis. For SEM analysis, a drop of each sample solution was applied to a 1 × 1 cm^2 silicon wafer with sequential drying. X-ray powder diffraction (XRD, Siemens D-500) as a rapid analytical technique was used for phase identification and crystal structure determination of a crystalline material. Herein, samples were prepared by dropping a dispersion on silicon substrates and moved into an airtight container to ensure that the solvent was completely evaporated. The XRD datas were collected from 25° to 80° 2θ at a rate of 0.58°/min at room temperature on a diffractometer using Co $K\alpha$ ($\lambda = 1.788\,965$ Å). The chemical structure of nanostructures was recorded using an inVia Raman microscope (Renishaw, UK). An argon ion laser at 785 nm was used as excitation source. The samples were placed in 1.0 mm (inside diameter) quartz capillaries. The experimental conditions were as follows: 1 mW power, a 100× objective microscope, 1 cm^{-1} spectral resolution, and 30 s × 3 collection time. The magnetism and M−H curves of nanostructures were obtained by a vibrating sample magnetometer (VSM, Lakeshore VSM 7407). The iron concentrations of nanostructures were measured with a classical C−A (absorbance versus iron concentration) calibration curve, which was established with the 1,10-phenanthroline spectrophotometric method on a UV−visible spectrophotometer (UV-3600, Shimadzu).[10]

Theoretical Calculation of the Magnetic Dipolar Parameter λ. Magnetic dipolar interaction, as a major type of attractive force, is considered to be an important factor for the crystal oriented aggregates.[11a] Specially, the magnetic dipolar parameter λ, defined as the ratio of the magnetic dipolar to thermal energies ($\lambda = U/E$), dominated by particle sizes and surfactant layer, determines the aggregation of smaller particles.[11a] The natural dipolar unit is defined as the following equation, $U = \mu^2/D^3$ (μ being the magnetic moment, D being the effective hard-sphere diameter, consisting of the core diameter and the thickness of the surfactant layer).[11b,c] The magnetic dipole moment of a single-domain sphere with radius (r) and bulk saturation magnetization (M_s) is $\mu = 4\pi r^3 M_s/3$.[11c] Herein, the M_s and density of bulk Mn−Zn ferrite are 140 emu/g and 4.54 g/cm^3, and the average thickness of main surfactant layer OA molecule, denoted by C_{18}, is approximately 1.8 nm.[11d−f] In addition, thermal energy (E) is given by $E = k_B T$, where k_B is the Boltzman constant ($1.380\,648\,8 \times 10^{-23}$ $m^2 \cdot kg \cdot s^{-2} \cdot K^{-1}$) and T is the temperature.[11g]

Heat Induction Measurements. Measurement of heat generation of ferrite nanostructures was carried out using a moderate/high radio frequency heating machine (Shuangping SPG-06-III). The samples at uniform concentration (1.0 mg of Fe/mL) were placed inside a copper coil under an alternating current magnetic field (ACMF) (the frequency were set for 390 and 780 kHz, and both the currents were set for 12 A, respectively). Specific absorption rate (SAR) is defined as the amount of heat generated per unit gram of magnetic material per unit time and is highly dependent on the field amplitude and frequency, dimensions of inductive coil, liquid carrier, composition, and size distribution of the nanostructures. It determines the heating ability of magnetic materials when an ACMF magnetic field is applied. The SAR values are calculated with the following formula[12]

$$\mathrm{SAR} = C\,\frac{\mathrm{d}T}{\mathrm{d}t}\,\frac{m_{\mathrm{s}}}{m_{\mathrm{m}}}$$

where C is the specific heat capacity of the suspension (specific heat capacity of isooctane is 247.32 $\mathrm{J{\cdot}K^{-1}{\cdot}mol^{-1}}$), $\mathrm{d}T/\mathrm{d}t$ is the initial slope of temperature versus time graph, m_{s} is the mass of the suspension, and m_{m} is the mass of the magnetic material in the suspension.

■ RESULTS AND DISCUSSION

Formation Mechanism of OA-Adjusted Spherical, Cubical, and Starlike Mn−Zn Ferrite Nanocrystals. We have made extensive use of TEM to characterize the morphology, size, and crystal orientation of Mn−Zn ferrite nanocrystals. The shape-dependent nanostructures are obtained by merely changing initial molar ratios of OA to OAm [initially 12:0 and finally 0:12, Figure S1 in the Supporting Information (SI)]. When the OA/OAm molar ratio is 10:2, nearly spherical nanocrystals (ca. 9 nm) are obtained. Contrastively, decreasing the OA/OAm ratios to 7:5 and 5:7 yield the cubical (ca. 11 nm) and starlike (ca. 16 nm) nanocrystals, respectively. Figure 1 shows the TEM and HRTEM images, the selective area electron diffraction (SAED) patterns, and the corresponding schematic diagram of structure models of representative spherical, cubical, and starlike nanocrystals. The measured lattice fringes of these nanocrystals are 0.296 nm, corresponding to the {220} lattice planes, while the facet is (100). The SAED patterns of spherical and starlike nanocrystals show clear diffraction rings, attributed to the randomness of particle orientations, which are consistent with the distinct (220), (311), (400), (511), and (440) XRD peaks (Figure 2A). For cubical nanocrystals, the XRD pattern shows a relatively intensified (400) peak, indicating that the (100) crystal face is the preferential orientation. Further SAED pattern observation reveals the clear and symmetrical arced spots indexed as (220), (400), and (440), confirming their perfect single crystalline structure. All of the above nanocrystals reveal the high-quality crystalline nature. The calculated maximum yields for spherical, cubical, and starlike nanocrystals are 89.3%, 91.5%, 93.8%. Their corresponding composition measured by EDS is shown in Figure S3 and Table S1 in the SI.

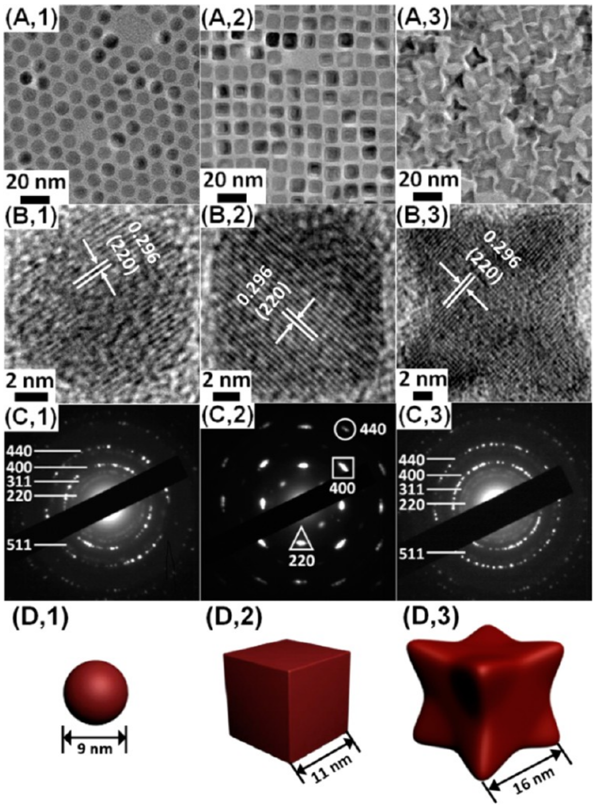

Figure 1. (A) TEM and (B) HRTEM images, (C) corresponding SAED patterns, and (D) schematic diagram of structure models of (1) spherical, (2) cubical, and (3) starlike Mn−Zn ferrite nanocrystals.

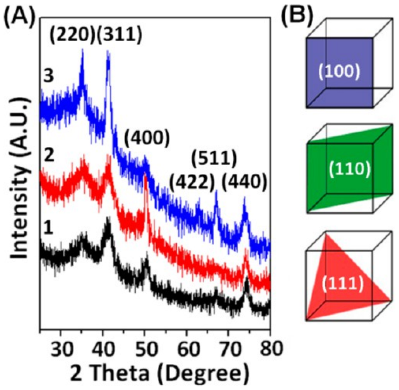

Figure 2. (A) XRD patterns with Co $K\alpha$ radiation on Si (100) substrates of (1) spherical, (2) cubical, and (3) starlike Mn−Zn ferrite nanocrystals. (B) The face-centered cubic (fcc) models with three low-energy facets.

Successes in similar starlike shape control of monodisperse $\mathrm{CoFe_2O_4}$ ferrites nanocrystals synthesized by high-temperature decomposition of mixed iron and cobalt oleates had been reported by Bao and co-workers.[3b] By controlling the process conditions, such as the concentration of precursors, heating rate, temperature, and the aging time, they found that the growth preference was an individual cubic intermediate corner or edges with higher surface energy and concentration of defects, leading to the eventual formation of an intricate starlike shape. Herein, a possible OA/OAm-adjusted shape formation mechanism of Mn−Zn ferrite nanocrystals is proposed. The OA with its carboxylic group bound strongly onto certain crystal facets of initial nuclei, forming a stabilizing layer to control the crystal growth rate.[6a,13] Contrastively, the OAm with an amine group has relatively weak binding onto the crystal surface.[6a,13] It is evident that the shape-controlled synthesis of nanocrystals might be achieved through the OA or OAm selective stabilization on specific crystal facets. When OA is sufficient during the nanocrystal growth, it can ensure that various crystal planes are well-capped and stablilized, the differential growth of crystal facets is negligible, thus leading to uniform spherical shape, as the case in Figure 1A,1. A small quantity of OAm as a crucial reducing agent here shows an inapparent effect on the morphology of nanocrystals.[6a] The typical spinel structure of ferrite nanocrystals is based on a face-centered cubic (fcc) model with three low-energy facets, {100}, {110}, and {111} (Figure 2B).[3c] The {100} planes show the lowest surface energy while the {111} planes have the highest.[3b,c] The weaker stabilization of OA on {111} facets with higher energy is available when insufficient amounts of OA are used. It induces the preferential growth along the [111] direction, resulting in the formation of cubical nanocrystals with the terminated {100} facets, as shown in Figure 1A,2. Furthermore, the continuous growth along the [111] directions leads to the eventual formation of starlike nanocrystals with eight corners symmetrically distributed around the cubical core when the amounts of OA are continuously decreasing (Figure 1A,3). It is worth mentioning that the OAm alone as a weak stabilizer can induce moderate stabilization on crystal faces, producing a lot of irregular-shaped nanocrystals with wide size distribution and poor uniformity (Figure S1H in the SI).

We have further investigated the dynamic shape evolution of as-synthesized spherical, cubical, and starlike nanocrystals. A small aliquot is rapidly withdrawn from the reaction solution at different durations for TEM analysis. As seen in Figure 3, the definite formation of nanocrystals is dependent on the reaction temperature and aging time. The crystal nucleation/growth process in synthesis is evaluated by the variation of the monomer concentration in the classical La Mer model.[3c,14] No product is observed for samples withdrawn from all reaction systems below 260 °C. Although the monomers, consisting of only a few initial "crystal units", might appear at this stage from decomposition of the precursor, it is difficult to observe them by using TEM. With continuous consumption of the monomer, the irregular "crystal nuclei" (2−3 nm) are formed at 260 °C. In the case of spherical nanocrystals synthesis (Figure 3A), the initial smaller-sized spheroidal nanocrystals arose subsequently at 260−300 °C. Finally, plenty of uniform spherical nanocrystals in a closed packed array are produced when prolonging the aging time from 20 to 40 min at 300 °C. In cubical and starlike nanocrystal synthesis, small quasispherical nanocrystals are first generated at the earlier durations (260−280 °C) (Figure 3B, C). At the beginning stage of the reaction at 300 °C, the product is primarily spherical with a small amount of quasicubical nanocrystals. Upon prolonging the aging time at 300 °C from 20 to 40 min, most of the nanocrystals continue growing to form uniform cubical nanocrystals accompanying the size variation (Figure 3B) or further grow along eight corners of intermediates, forming the starlike nanocrystals (Figure 3C). The continuous shape evolution of nanocrystals from the primal sphericity and cubicity to the final starriness can be successfully observed by adjusting OA/OAm ratios, as schematically illustrated in Figure 3D.

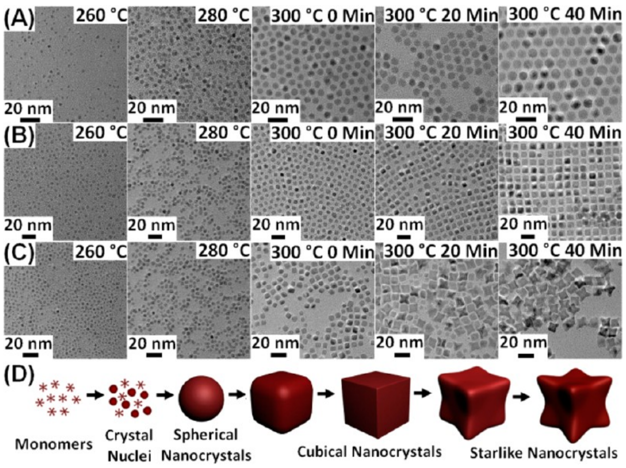

Figure 3. TEM images of (A) spherical, (B) cubical, and (C) starlike Mn−Zn ferrite nanocrystals withdrawn from the reaction solution at 260, 280, and 300 °C after aging for 0, 20, and 40 min. (D) Schematic illustration of the starlike nanocrystals shape evolution.

Formation Mechanism of Self-Assembled Mn−Zn Ferrite Nanoclusters. It is interesting that the regulation of nucleation and growth process may tailor the morphology of Mn−Zn ferrite nanostructures in surfactant-assisted synthesis. In the case of 5 mmol of OA and 7 mmol of OAm, the self-assembled nanoclusters are obtained by adopting a short nucleation time at 220 °C (nucleation temperature) and aging at 300 °C (maturation temperature) for different duration times. The formation process of the nanoclusters is observed by TEM [Figures S4 (SI), 4, and 5]. At the stage of 220 °C, the decrease of nucleation time induces the lower amounts of initial "crystal nuclei" in the system, leading to a deficient nucleation. It might bring a rapid increase in monomer concentration, which accelerates the subsequent growth process of nanocrystals, leading to the formation of final starlike nanocrystals in

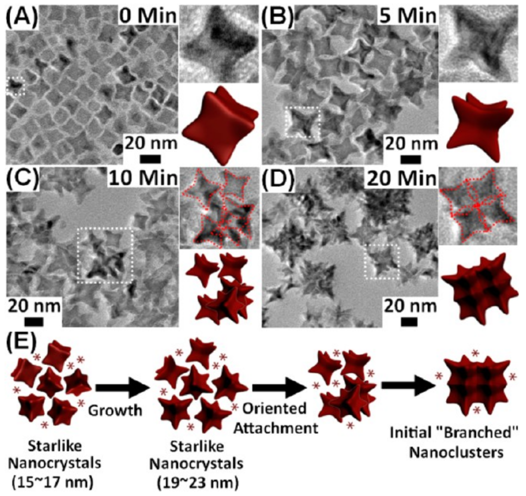

Figure 4. (A−D) TEM images of Mn−Zn ferrite nanoclusters withdrawn from the reaction solution at 300 °C after aging for 0, 5, 10, and 20 min. (E) Schematic illustration of the transformation of nanocrystals into nanoclusters.

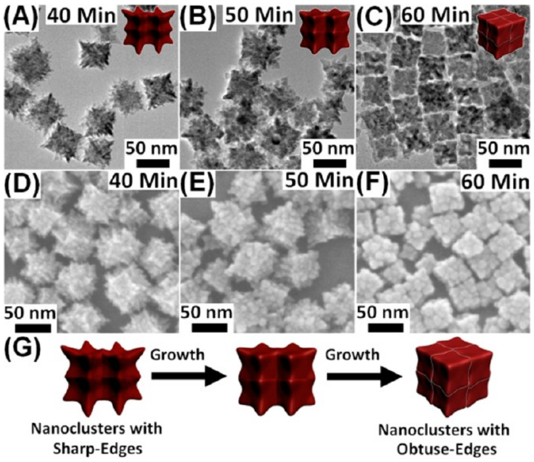

Figure 5. (A−C) TEM and (D−F) SEM images of Mn−Zn ferrite nanoclusters withdrawn from the reaction solution at 300 °C after aging for 40, 50, and 60 min. (G) Schematic illustration of the transformation of sharp-edged nanoclusters into obtuse-edged nanoclusters.

larger size (ca. 19−23 nm) at 300 °C after aging for 5 min (Figure 4B). This process is in accord with above-mentioned OA-assisted nucleation and growth of 0-D nanostars. It is worthwhile to note that the 19−23 nm-sized starlike nanocrystals are oriented to assemble reciprocally, gradually forming initial aggregated 3-D "branched" nanoclusters (ca. 30−40 nm) at 300 °C aging for 10−20 min (Figures 4C,D and S5 in the SI). Owing to the "particle coalescence" effects,[2d] the sizes of proposed starlike basic units of formed nanoclusters are distinctly decreased. For previous $CoFe_2O_4$ ferrites synthesis, researchers found that the introduction of boiling bursts by injection of a small amount of hexane during the heating cycle, accompanied by a temperature drop, could slow down the growth of the nuclei and promote their oriented attachments by the interaction between the nuclei.[2d]

Generally, magnetic nanocrystals dispersed in solution are subjected to two major types of attractive forces: isotropic van der Waals and anisotropic magnetic dipolar interactions.[15a] The magnetic dipolar interaction has the stronger volume dependence, scales as μ^2/D^3 or r^6/D^3 (see the Experimental Section). Comparatively, the van der Waals interaction is a function of r/D only. The van der Waals attractions will become relatively less important on increasing the particle size, whereas dipolar interaction is very sensitive to particle radius, which is clearly observed above a critical particle size.[15c] Herein, the produced 19−23-nm-sized starlike nanocrystals are coated with a relatively thick surfactant layer (C_{18}, $d = 1.8$ nm) to minimize the effect of van der Waals attractions. The strength of the magnetic dipolar moments plays a fundamental factor in controlling the oriented aggregation of starlike nanocrystals. We have calculated the dipolar parameter λ to be 0.37, 0.80, 3.11 for as-synthesized spherical, cubical and starlike nanocrystals (ca. 9, 11, 16 nm), which are smaller than or comparable to the threshold λ value of about 3 for aggregate formation.[15a] So no particles assemblies are observed in these nanocrystals synthesis. Moreover, the calculated λ value for 19−23-nm-sized starlike nanocrystals is 5.70−10.99. It exhibits strong size-dependent magnetic dipolar interactions, promoting the formation of nanoclusters to minimize their magnetostatic energy.

In addition, the defect-induced secondary growth of both the starlike nanocrystals and subsequently formed nanoclusters is possible due to the high monomer concentration in the reaction system. As direct evidence, we can observe several irregular or floccular nanostructures caused by secondary growth of nanostars (Figures 4B,C). When prolonging the growth time at 300 °C to 40 min, the uniformity of the "branched" nanoclusters is considerably improved, accompanied by the size increase. This is attributed to the continuous secondary growth of initial nanoclusters, leading to the final larger-sized "multibranched" nanoclusters (ca. 50 nm) with sharp edges (Figure 5A,D). The transformation of nanocrystals into nanoclusters depending on the oriented aggregation and secondary growth of nanostructures is expatiated in Figure 4E.

The nanoclusters with sharp edges (ca. 50 nm) become the dominating species at this stage (Figure 5A,D). But interestingly, the passivation of sharp edges on the surface of nanoclusters is observed at 300 °C aging for 40−60 min (Figure 5B,E). It is probable that the assembled crystals on the sharp edges of nanoclusters fuse together to form a more densely packed and steady structure with lower surface energy,[2d] which successfully tend to convert to nanoclusters with obtuse edges (ca. 45 nm, 300 °C aging for 60 min, Figure 5C,F). The schematic illustration of the multibranched nanoclusters transformation is provided in Figure 5G.

Figures 6 and 6S (SI) show the SEM, TEM, and HRTEM images of two representative purified and highly ordered sharp- and obtuse-edged Mn−Zn ferrite nanoclusters with uniform sizes, obtained for different maturation times. Two distinct lattice spacings at the corner regions of nanoclusters, measured to be 0.206 and 0.296 nm, correspond to the (400) and (220) planes. Comparing with perfect fcc-structured 0-D nanocrystals (Figure 1), generally exhibiting only {100} facets, these 3-D nanoclusters possess more complex configuration, including multiple crystal facets, a mass of sharp or obtuse edges, and large surface areas. The composition of the ferrite nanoclusters measured by EDS is shown in Figure S7 and Table S2 in the SI, and the calculated maximum yields are 80.4% and 78.6%. The removing of small-sized particles and uncompletely reacted substance may bring considerable losses in the centrifugation and washing processes.

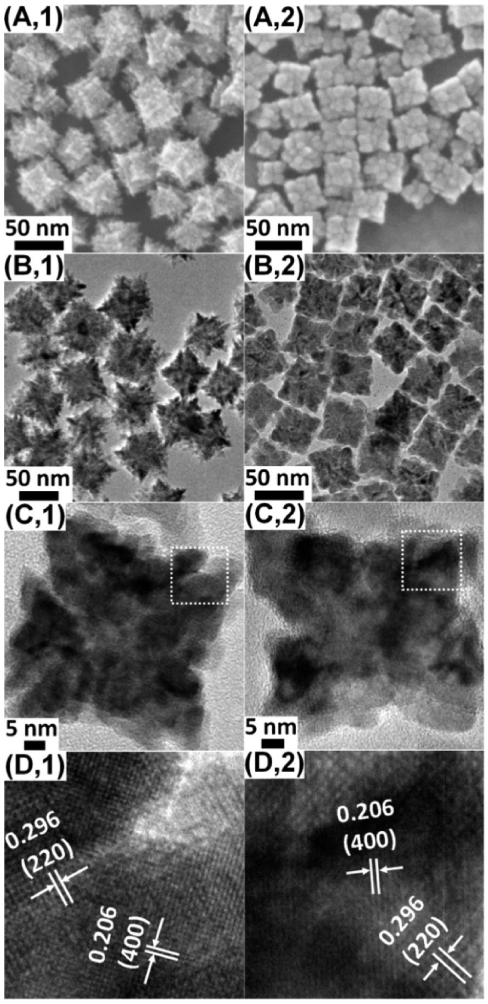

Figure 6. (A) SEM, (B) TEM, and (C, D) HRTEM images of Mn−Zn ferrite nanoclusters with (1) sharp and (2) obtuse edges.

Furthermore, the detailed crystallization process of above-mentioned multibranched nanoclusters at different reaction temperatures, including the occurrence of nucleation, growth, coarsening, and agglomeration, is investigated by studying the XRD peaks, which is shown in Figure 7A. No significant diffraction peaks are observed at the initial nucleation stage

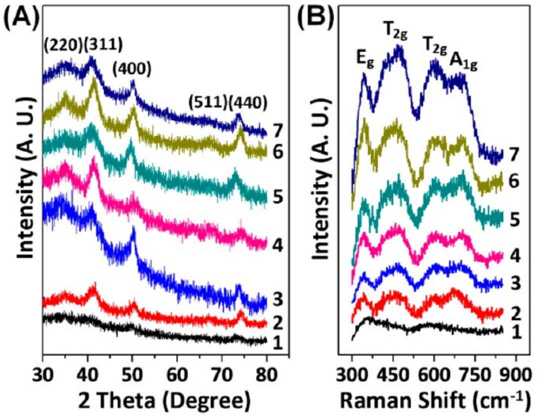

Figure 7. (A) XRD patterns with Co Kα radiation on Si (100) substrates and (B) Raman spectroscopy of Mn−Zn ferrite nanoclusters withdrawn from the reaction solution at (1) 220 °C, (2) 240 °C, (3) 280 °C, and 300 °C after aging for (4) 0 min, (5) 20 min, (6) 40 min, and (7) 60 min.

[220 °C, Sample 1 (S1)], because the crystallinity of the "crystal units" sample is greatly weak. At the heating temperature of 240 °C (S2), some peaks assigned to the (311), (400), and (440) diffraction planes vaguely appear, respectively. Upon the temperature of 280 °C (S3−S7), the crystallinity of samples is clear, which is displayed by the sharp diffraction patterns. For the two representative nanoclusters with sharp and obtuse edges, the major XRD peaks can be indexed as (220), (311), (400), (511), and (440) planes (S6, S7), which match well with a spinel ferrite structure.

Raman spectroscopy is an important technique that can provide useful information about the internal structure, chemical bonding, crystallization degrees, and phase transition of materials ranging from bulk to nanoscale crystals.[16] Figure 7B shows the Raman spectra evolution of Mn−Zn ferrite nanoclusters during the heating process, in the temperature range from 220 to 300 °C. The theoretical analysis for spinel magnetite (Fe_3O_4) shows that there are five Raman active modes (A_{1g} + E_g + $3T_{2g}$) in the range 200−800 cm^{-1}, which involve mainly the motion of the oxygen ions and both the oxygen and metal ions.[16a] The observed main Raman vibration modes that occurred in our Mn−Zn ferrite samples can be assigned as T_{2g} symmetry (442−445, 592−595 cm^{-1}), E_g (343−346 cm^{-1}), A_{1g} (670−705 cm^{-1}),[16b,c] which are listed in Table 1. The initial crystallization stage (220 °C, S1) shows a broad and weak Raman signature of samples. Raman band broadening is intrinsic to many smaller-sized or defective nanophased oxides.[16d−f] In the nucleation and initial growth process of the "crystal units", lots of structural oxygen or cation related defects are present in the crystal surface, resulting in the disorder of the lattice structure. In this case, the structural fluctuations may cause phonon geometrical scattering, shorten the phonon mean lifetime, and change the corresponding phonon vibration frequency, which account for the anomalous peak broadening observed.[16d] In the following growth and aggregation process of nanocrystals (240−300 °C), fewer structural defects occur in these samples, accompanied by the improvements of the crystallinity. So the resulting Raman peak widths become gradually narrowing and sharp (S6, S7).

Table 1. Assignment of Raman Modes of Mn−Zn Ferrite Samples and Reported Fe_3O_4 Crystal

	Raman spectra (cm^{-1})	
assignment	sample 1−7	Fe_3O_4 crystal[16a]
$T_{2g\ (1)}$	–	193
E_g	343−346	306
$T_{2g\ (2)}$	442−445	450−490
$T_{2g\ (3)}$	592−595	538
A_{1g}	670−705	668

[a] Sample 1−7: Mn−Zn ferrite nanoclusters withdrawn from the reaction solution at (1) 220 °C, (2) 240 °C, (3) 280 °C, and 300 °C after aging for (4) 0 min, (5) 20 min, (6) 40 min, and (7) 60 min.

Magnetic Characteristic. Magnetic characteristic is crucial for the successful Mn−Zn ferrite nanostructures, which is directly related to their biomedical applications.[1,2,4] The important parameters for the magnetism modulation of nanostructures are their size aggregation, crystallinity, and composition.[2,4] Using VSM, the hysteresis loops of our all samples at room temperature (300 K) are measured, giving varying M_s values of 78.3 and 82.5 emu/g Fe for Mn−Zn ferrite nanoclusters with sharp and obtuse edges (Figure 8A) and 32.2, 43.5, 51.7 emu/g Fe for foregoing spherical, cubical, and starlike nanocrystals (Figure S8, SI), respectively. Almost no coercivity (H_C) and remnant magnetization are observed for the above five types of nanostructures, exhibiting their superparamagnetic behaviors. For individual nanocrystals, the lower magnetization may be due to their smaller magnetic cores, limiting their usage in effective manipulation in moderate

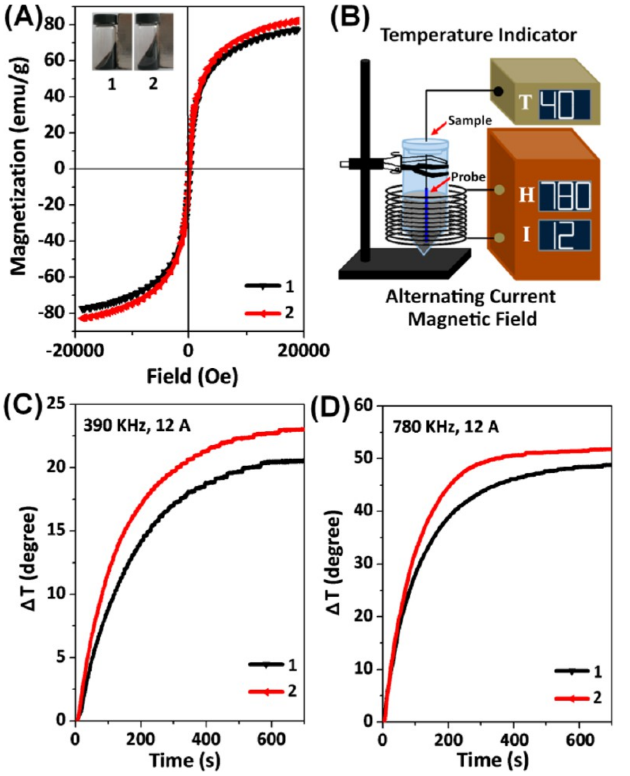

Figure 8. (A) Hysteresis loops of Mn−Zn ferrite nanoclusters with (1) sharp and (2) obtuse edges. The inset shows the digital images of samples. (B) Experimental simulation of magnetically induced heating effects and (C, D) time−temperature curves of Mn−Zn ferrite nanoclusters with (1) sharp edges and (2) obtuse edges in isooctane phase (1 mg of Fe/mL) under ACMF, in which the frequencies are 390 and 780 kHz and both currents are 12 A.

AMF. For nanoclusters, a distinct improvement in magnetism may be attributed to their larger-sized aggregation formation. These nanoclusters composed of a number of small-sized primary crystals have the advantage of controllably increased magnetic coupling while retaining superparamagnetic characteristics, even though their size exceeds 40 nm. Surprisingly, the magnetism of 50-nm-sized sharp-edged nanoclusters is lower than that of 45-nm-sized obtuse-edged nanoclusters. Compared to the loose structure of sharp-edged nanoclusters, obtuse-edged nanoclusters have more densely packed structure, resulting in the enhanced magnetic moment, which may be responsible for higher magnetization.

Magnetically Induced Heating Efficiency in ACMF. The excellent magnetic properties of Mn−Zn ferrite nanostructures can also be used to achieve magnetically induced heating in an ACMF (Figure 8B). The SAR value as a standard criterion is highly dependent on magnetic relaxation and is proportional to the value of M_s. For five types of as-synthesized nanostructures at uniform concentration of 1.0 mg of Fe/mL, the temperature rising curves in ACMF (390 and 780 kHz, 12 A) are presented in Figures 8C, D and S9 (SI), and the calculated SAR values in isooctane are established in Tables 2 and S3 (SI). It is found that the Mn−Zn ferrite nanoclusters with sharp and obtuse edges possess higher SAR values (201.1 and 225.5 W/g for 390 kHz and 482.6 and 513.2 W/g for 780 kHz), which are 1.5 times higher than that of the Fe_3O_4 nanoclusters with similar morphologies and sizes synthesized in identical conditions (Figure S10 in SI). The peculiar structure (multimagnetic core assemblies with larger sizes) of the Mn−Zn ferrite nanoclusters contributed to their enhanced heating capacity, which is consistent with the saturation magnetization above. The higher SAR values of nanoclusters mean that the optimization of their heating effects is possible to reach and maintain temperatures around 42 °C, which can be potentially applied in cancer hyperthermia in vivo.

Table 2. Calculated SAR Values, M_S, and Size of Sharp- and Obtuse-Edged Nanoclusters

samples	sharp-edged nanocluster		obtuse-edged nanocluster	
frequency (kHz)	390	780	390	780
calcd SAR (W/g)	201.1	482.6	225.5	513.2
M_s (emu/g)	78.3		82.5	
size (nm)	50		45	

CONCLUSION

In summary, we have synthesized the monodisperse Mn−Zn ferrite nanocrystals and nanoclusters with various morphologies. The strong surfactant effect and differential stabilization of OA lead to the formation of 0-D spherical, cubical, and starlike nanocrystals. Furthermore, the highly ordered, self-assembled 3-D nanoclusters with sharp and obtuse edges are fabricated by controlling the nucleation and growth dynamics. The formation of stable nanoclusters is subjected to three major processes: (i) classical nucleation and growth of the nanocrystals, (ii) highly oriented aggregation between the nanocrystals, and (iii) defect-induced secondary growth of initial branched aggregation. The main driving force for their oriented attachments is size-dependent magnetic dipolar interactions of individual nanocrystals. We believe that the outstanding magnetic performances make the nanoclusters promising as excellent heating agents for hyperthermia in vivo in further biomedical application.

ASSOCIATED CONTENT

Ⓢ Supporting Information

Figures S1−S10 and Tables S1−S3. This material is available free of charge via the Internet at http://pubs.acs.org.

AUTHOR INFORMATION

Corresponding Author

*E-mail: zhangyu@seu.edu.cn.

Notes

The authors declare no competing financial interest

ACKNOWLEDGMENTS

This research was supported by the National Basic Research Program of China (No. 2011CB933503, 2013CB733800), National Natural Science Foundation of China (No. 31170959, 81071445), the Basic Research Program of Jiangsu Province (Natural Science Foundation, No. BK2011036), and National Key Technology Research and Development Program of China (2012BAI23B02).

REFERENCES

(1) (a) Jun, Y. W.; Lee, J. H.; Cheon, J. *Angew. Chem., Int. Ed.* **2008**, *47*, 5122−5135. (b) Lee, J. H.; Jang, J. T.; Choi, J. S.; Moon, S. H.; Noh, S. H.; Kim, J. W.; Kim, J. G.; Kim, I. S.; Park, K. I.; Cheon, J. *Nat. Nanotechnol.* **2011**, *26*, 418−422. (c) Yoo, D.; Lee, J. H.; Shin, T. H.; Cheon, J. *Acc. Chem. Res.* **2011**, *44*, 863−874. (d) Chen, Z. W.; Yin, J. J.; Zhou, Y. T.; Zhang, Y.; Song, L. N.; Song, M. J.; Hu, S. L.; Gu, N. *ASC Nano* **2012**, *6*, 4001−4012.

(2) (a) Jia, C. J.; Sun, L. D.; Luo, F.; Han, X. D.; Heyderman, L. J.; Yan, Z. G.; Yan, C. H.; Zheng, K.; Zhang, Z.; Takano, M.; Hayashi, N.; Eltschka, M.; Kläui, M.; Rüdiger, U.; Kasama, T.; Cervera-Gontard, L.; Dunin-Borkowski, R. E.; Tzvetkov, G.; Raabe, J. *J. Am. Chem. Soc.* **2008**, *130*, 16968−16977. (b) Cheon, J.; Kang, N. J.; Lee, S. M.; Lee, J. H.; Yoon, J. H.; Oh, S. J. *J. Am. Chem. Soc.* **2004**, *126*, 1950−1951. (c) Lee, N.; Choi, Y.; Lee, Y.; Park, M.; Moon, W. K.; Choi, S. H.; Hyeon, T. *Nano Lett.* **2012**, *12*, 3127−3131. (d) Bao, N. Z.; Shen, L. M.; Wang, Y. H. A.; Ma, J. X.; Mazumdar, D.; Gupta, A. *J. Am. Chem. Soc.* **2009**, *131*, 12900−12901.

(3) (a) Jun, Y. W.; Choi, J. S.; Cheon, J. *Angew. Chem., Int. Ed.* **2006**, *45*, 3414−3439. (b) Bao, N. Z.; Shen, L. M.; An, W.; Padhan, P.; Turner, C. H.; Gupta, A. *Chem. Mater.* **2009**, *21*, 3458−3468. (c) Ho, C. H.; Tsai, C. P.; Chung, C. C.; Tsai, C. Y.; Chen, F. R.; Lin, H. J.; Lai, C. H. *Chem. Mater.* **2011**, *23*, 1753−1760. (d) Zhen, G. L.; Muir, B. W.; Moffat, B. A.; Harbour, P.; Murray, K. S.; Moubaraki, B.; Suzuki, K.; Madsen, I.; Agron-Olshina, N.; Waddington, L.; Mulvaney, P.; Hartley, P. G. *J. Phys. Chem. C* **2011**, *115*, 327−334. (e) Zeng, H.; Rice, P. M.; Wang, S. X.; Sun, S. H. *J. Am. Chem. Soc.* **2004**, *126*, 11458−11459.

(4) (a) de la Presa, P.; Luengo, Y.; Multigner, M.; Costo, R.; Morales, M. P.; Rivero, G.; Hernando, A. *J. Phys. Chem. C* **2012**, *116*, 25602−25610. (b) Ho, D.; Sun, X. L.; Sun, S. H. *Acc. Chem. Res.* **2011**, *44*, 875−882.

(5) (a) Ge, J. P.; Hu, Y. X.; Biasini, M.; Beyermann, W. P.; Yin, Y. D. *Angew. Chem., Int. Ed.* **2007**, *46*, 4342−4345. (b) Hugounenq, P.; Levy, M.; Alloyeau, D.; Lartigue, L.; Dubois, E.; Cabuil, V.; Ricolleau, C.; Roux, S.; Wilhelm, C.; Gazeau, F.; Bazzi, R. *J. Phys. Chem. C* **2012**, *116*, 15702−15712. (c) Xu, F. J.; Cheng, C. M.; Chen, D. X.; Gu, H. C. *ChemPhysChem.* **2012**, *13*, 336−341.

(6) (a) Gao, G. H.; Liu, X. H.; Shi, R. R.; Zhou, K. C.; Shi, Y. G.; Ma, R. Z.; Takayama-Muromachi, E.; Qiu, G. Z. *Cryst. Growth Des.* **2010**, *10*, 2888−2894. (b) Kovalenko, M. V.; Bodnarchuk, M. I.; Lechner, R. T.; Hesser, G.; Schäffler, F.; Heiss, W. *J. Am. Chem. Soc.* **2007**, *129*,

6352−6353. (c) Xie, J.; Peng, S.; Brower, N.; Pourmand, N.; Wang, S. X.; Sun, S. H. *Pure Appl. Chem.* **2006**, *78*, 1003−1014.

(7) (a) Hu, M.; Jiang, J. S. *CrystEngComm* **2010**, *12*, 3391−3393. (b) Zhang, J.; Huang, F.; Lin, Z. *Nanoscale* **2010**, *2*, 18−34. (c) Zhuang, Z. Y.; Huang, F.; Lin, Z.; Zhang, H. Z. *J. Am. Chem. Soc.* **2012**, *134*, 16228−16234.

(8) (a) Sun, S. H.; Zeng, H.; Robinson, D. B.; Raoux, S.; Rice, P. M.; Wang, S. X.; Li, G. X. *J. Am. Chem. Soc.* **2004**, *126*, 273−279. (b) Frey, N. A.; Peng, S.; Cheng, K.; Sun, S. H. *Chem. Soc. Rev.* **2009**, *38*, 2532−2542. (c) Sun, S. H.; Zeng, H. *J. Am. Chem. Soc.* **2002**, *124*, 8204−8205.

(9) (a) Jang, J. T.; Nah, H.; Lee, J. H.; Moon, S. H.; Kim, M. G.; Cheon. *J. Angew. Chem. Int. Ed.* **2009**, *48*, 1234−1238. (b) Kim, D. H.; Nikles, D. E.; Brazel, C. S. *Materials* **2010**, *3*, 4051−4065.

(10) Harvey, A. E., Jr.; Smart, J. A.; Amis, E. S. *Anal. Chem.* **1955**, *27*, 26−29.

(11) (a) Lalatonne, Y.; Richardi, J.; Pileni, M. P. *Nat. Mater.* **2004**, *3*, 121−125. (b) Tlusty, T.; Safran, S. A. *Science* **2000**, *290*, 1328−1331. (c) Butter, K.; Bomans, P. H. H.; Frederik, P. M.; Vroege, G. J.; Philipse, A. P. *Nat. Mater.* **2003**, *2*, 88−91. (d) Waqas, H.; Qureshi, A. H. *J. Therm. Anal. Calorim.* **2010**, *100*, 529−535. (e) Topfer, J.; Angermann, A. *Mater. Chem. Phys.* **2011**, *129*, 337−342. (f) Angermann, A.; Hartmann, E.; Topfer, J. *J. Magn. Magn. Mater.* **2010**, *322*, 3455−3459. (g) Puntes, V. F.; Krishnan, K. M.; Alivisatos, A. P. *Science* **2001**, *291*, 2115−2117.

(12) Babincová, M.; Leszczynska, D.; Sourivong, P.; Čičmanec, P.; Babinec, P. *J. Magn. Magn. Mater.* **2005**, *225*, 109−112.

(13) (a) Yang, C.; Wu, J. J.; Hou, Y. L. *Chem. Commun.* **2011**, *47*, 5130−5141. (b) Yang, H. T.; Hasegawa, D.; Takahashi, M.; Ogawa, T. *IEEE Trans. Magn.* **2008**, *44*, 3895−3898. (c) Hou, Y. L.; Xu, Z. C.; Sun, S. H. *Angew. Chem.* **2007**, *119*, 6445−6448.

(14) (a) LaMer, V. K.; Dinegar, R. H. *J. Am. Chem. Soc.* **1950**, *72*, 4847−4854. (b) Murray, C. B.; Kagan, C. R.; Bawendi, M. G. *Annu. Rev. Mater. Sci.* **2000**, *30*, 545−610.

(15) (a) Lalatonne, Y.; Richardi, J.; Pileni, M. P. *Nat. Mater.* **2004**, *3*, 121−125. (b) Tlusty, T.; Safran, S. A. *Science* **2000**, *290*, 1328−1331. (c) Butter, K.; Bomans, P. H. H.; Frederik, P. M.; Vroege, G. J.; Philipse, A. P. *Nat. Mater.* **2003**, *2*, 88−91. (d) Puntes, V. F.; Krishnan, K. M.; Alivisatos, A. P. *Science* **2001**, *291*, 2115−2117.

(16) (a) Shebanova, O. N.; Lazor, P. *J. Solid State Chem.* **2003**, *174*, 424−430. (b) Yamashita, O.; Ikeda, T. *J. Appl. Phys.* **2004**, *95*, 1743−1748. (c) Varshney, D.; Verma, K.; Kumar, A. *Mater. Chem. Phys.* **2011**, *131*, 413−419. (d) Zhao, S. Y.; Shi, L.; Zhou, S. M.; Zhao, J. Y.; Yang, H. P.; Guo, Y. Q. *J. Appl. Phys.* **2009**, *106*, 123901. (e) Choi, H. C.; Jung, Y. M.; Kim, S. B. *Vib. Spectrosc.* **2005**, *37*, 33−38. (f) Cvejic, Z.; Rakic, S.; Kremenovic, A.; Antic, B.; Jovalekic, C.; Colomban, P. *Solid State Sci.* **2006**, *8*, 908−915. (g) de Faria, D. L. A.; Silva, S. V.; de Oliveira, M. T. J. *Raman Spectrosc.* **1997**, *28*, 873−878. (h) Chamritski, I.; Burns, G. *J. Phys. Chem. B* **2005**, *109*, 4965−4968.